The Astrophysical Journal Letters, 969:L9 (13pp), 2024 July 1 https://doi.org/10.3847/2041-8213/ad5186
© 2024. The Author(s). Published by the American Astronomical Society.
OPEN ACCESS

Shockingly Bright Warm Carbon Monoxide Molecular Features in the Supernova Remnant Cassiopeia A Revealed by JWST

J. Rho[1,2], S.-H. Park[2], R. Arendt[3,4], M. Matsuura[5], D. Milisavljevic[6], T. Temim[7], I. De Looze[8], W. P. Blair[9], A. Rest[9,10], O. Fox[10], A. P. Ravi[11], B.-C. Koo[2], M. Barlow[12], A. Burrows[7], R. Chevalier[13], G. Clayton[14], R. Fesen[15], C. Fransson[16], C. Fryer[17], H. L. Gomez[18], H.-T. Janka[19], F. Kirchschlager[8], J. M. Laming[20], S. Orlando[21], D. Patnaude[22], G. Pavlov[23], P. Plucinsky[22], B. Posselt[24], F. Priestley[18], J. Raymond[22], N. Sartorio[8], F. Schmidt[12], P. Slane[22], N. Smith[25], N. Sravan[26], J. Vink[27], K. Weil[28], J. Wheeler[29], and S. C. Yoon[2]
[1] SETI Institute, 189 Bernardo Avenue, Ste. 200, Mountain View, CA 94043, USA; jrho@seti.org
[2] Department of Physics and Astronomy, Seoul National University, Gwanak-ro 1, Gwanak-gu, Seoul 08826, Republic of Korea
[3] Center for Space Sciences and Technology, University of Maryland, Baltimore County, Baltimore, MD 21250, USA
[4] Code 665, NASA/GSFC, 8800 Greenbelt Road, Greenbelt, MD 20771, USA
[5] Cardiff Hub for Astrophysics Research and Technology (CHART), School of Physics and Astronomy, Cardiff University, The Parade, Cardiff CF24 3AA, UK
[6] Department of Physics and Astronomy, Purdue University, 525 Northwestern Avenue, West Lafayette, IN 47907, USA
[7] Department of Astrophysical Sciences, Princeton University, Princeton, NJ 08544, USA
[8] Sterrenkundig Observatorium, Ghent University, Krijgslaan 281-S9, B-9000 Ghent, Belgium
[9] William H. Miller III Department of Physics and Astronomy, Johns Hopkins University, 3400 N. Charles Street, Baltimore, MD 21218, USA
[10] Space Telescope Science Institute, 3700 San Martin Drive, Baltimore, MD 21218, USA
[11] Department of Physics and Astronomy, University of California, 1 Shields Avenue, Davis, CA 95616-5270, USA
[12] Department of Physics and Astronomy, University College London, Gower Street, London WC1E 6BT, UK
[13] Department of Astronomy, University of Virginia, Charlottesville, VA 22904-4325, USA
[14] Department of Physics & Astronomy, Louisiana State University, Baton Rouge, LA 70803, USA
[15] 6127 Wilder Lab, Department of Physics and Astronomy, Dartmouth College, Hanover, NH 03755, USA
[16] Department of Astronomy, Stockholm University, The Oskar Klein Centre, AlbaNova, SE-106 91 Stockholm, Sweden
[17] Center for Nonlinear Studies, Los Alamos National Laboratory, Los Alamos, NM 87545, USA
[18] Cardiff Hub for Astrophysical Research and Technology (CHART), School of Physics & Astronomy, Cardiff University, The Parade, Cardiff, CF24 3AA, UK
[19] Max Planck Institute for Astrophysics, Karl-Schwarzschild-Str. 1, 85748 Garching, Germany
[20] Space Science Division, Code 7684, Naval Research Laboratory, Washington DC 20375, USA
[21] INAF—Osservatorio Astronomico di Palermo, Piazza del Parlamento 1, 90134 Palermo, Italy
[22] Center for Astrophysics | Harvard & Smithsonian, 60 Garden Street, Cambridge, MA 02138, USA
[23] Pennsylvania State University, Department of Astronomy & Astrophysics, 525 Davey Lab., University Park, PA 16802, USA
[24] Oxford Astrophysics, University of Oxford, Denys Wilkinson Building, Keble Road, Oxford, OX1 3RH, UK
[25] Steward Observatory, University of Arizona, 933 N. Cherry Avenue, Tucson, AZ 85721, USA
[26] Department of Physics, Drexel University, Philadelphia, PA 19104, USA
[27] Anton Pannekoek Institute for Astronomy & GRAPPA, University of Amsterdam, Science Park 904, 1098 XH Amsterdam, The Netherlands
[28] Department of Physics and Astronomy, 6127 Wilder Laboratory, Dartmouth College, Hanover, NH 03755, USA
[29] University of Texas at Austin, 1 University Station C1400, Austin, TX 78712-0259, USA
Received 2024 February 26; revised 2024 May 27; accepted 2024 May 27; published 2024 June 24

Abstract

We present JWST NIRCam (F356W and F444W filters) and MIRI (F770W) images and NIRSpec Integral Field Unit (IFU) spectroscopy of the young Galactic supernova remnant Cassiopeia A (Cas A) to probe the physical conditions for molecular CO formation and destruction in supernova ejecta. We obtained the data as part of a JWST survey of Cas A. The NIRCam and MIRI images map the spatial distributions of synchrotron radiation, Ar-rich ejecta, and CO on both large and small scales, revealing remarkably complex structures. The CO emission is stronger at the outer layers than the Ar ejecta, which indicates the re-formation of CO molecules behind the reverse shock. NIRSpec-IFU spectra (3–5.5 μm) were obtained toward two representative knots in the NE and S fields that show very different nucleosynthesis characteristics. Both regions are dominated by the bright fundamental rovibrational band of CO in the two R and P branches, with strong [Ar VI] and relatively weaker, variable strength ejecta lines of [Si IX], [Ca IV], [Ca V], and [Mg IV]. The NIRSpec-IFU data resolve individual ejecta knots and filaments spatially and in velocity space. The fundamental CO band in the JWST spectra reveals unique shapes of CO, showing a few tens of sinusoidal patterns of rovibrational lines with pseudocontinuum underneath, which is attributed to the high-velocity widths of CO lines. Our results with LTE modeling of CO emission indicate a temperature of $\sim$1080 K and provide unique insight into the correlations between dust, molecules, and highly ionized ejecta in supernovae and have strong ramifications for modeling dust formation that is led by CO cooling in the early Universe.

Unified Astronomy Thesaurus concepts: Supernova remnants (1667); Metal-containing molecules (2258); CO line emission (262); Supernovae (1668); James Webb Space Telescope (2291); Ejecta (453); Astrochemistry (75); Dust formation (2269)

Original content from this work may be used under the terms of the Creative Commons Attribution 4.0 licence. Any further distribution of this work must maintain attribution to the author(s) and the title of the work, journal citation and DOI.

1. Introduction

The large amounts of dust seen in some high-z galaxies imply that dust formed in the early Universe. However, intermediate-mass stars, thought to produce most interstellar

dust when on the asymptotic giant branch in present-day galaxies (Laporte et al. 2017), would not have evolved to the dust-producing stage in high-z galaxies. In contrast, core-collapse supernovae (ccSNe) from high-mass stars occur just several million years after their progenitors are born and have also been suggested to be molecular factories in the early Universe (Cherchneff & Lilly 2008). Molecules, e.g., carbon monoxide (CO), are the signature of the onset of dust formation since they are one of the ejecta's most powerful coolants (Cherchneff & Lilly 2008) at temperatures where dust can form.

However, whether SNe are a significant (if not dominant) source of dust in the early Universe has been and continues to be debated (e.g., Nozawa et al. 2006; Cherchneff & Dwek 2009). The dust masses observed in ccSNe within a few years after their explosions are less than 0.01 $M_{\odot}$, a value that is far too small to explain the amount of dust observed in the early Universe (Kotak et al. 2009; Gall et al. 2011; Tinyanont et al. 2019). In contrast, Herschel and Spitzer observations of a few young supernova remnants (SNRs), including SN 1987A (20 yr; Matsuura et al. 2011) and Cas A (∼350 yr), have dust masses of 0.1–1 $M_{\odot}$ (Rho et al. 2018b; Millard et al. 2021; Matsuura et al. 2015; Chawner et al. 2019; De Looze et al. 2017, and references therein), which is in agreement with dust formation models (Nozawa et al. 2003; Todini & Ferrara 2001; Sluder et al. 2018) that suggest that SNe could be major dust factories at high-z galaxies (Dwek & Cherchneff 2011).

The cause of discrepancies in the measured dust masses from early to later phases and the timescale of dust formation are under debate. Recently, Niculescu-Duvaz et al. (2022) and Shahbandeh et al. (2023) suggested that a dust mass grows with time and most dust forms at times >3 yr after the explosion, while Dwek et al. (2019) suggest that the dust forms early in optically thick clumps and only a fraction of its IR emission is detected due to high IR opacity.

Dust may undergo complete or partial destruction following its initial formation, which depends on shock velocity and grain size (Slavin et al. 2020), potentially altering the expected dust grain size distribution in the process. When the forward shock of a supernova (SN) accumulates sufficient pressure at the SN shell, a second shock (called a reverse shock) develops in the interior (Chevalier 1977; Borkowski & Shull 1990). The dust (or ejecta) destruction by the passage through the reverse shock of ccSNe depends on grain composition, grain size distribution, and the shock properties (Priestley et al. 2021; Nozawa et al. 2007; Kirchschlager et al. 2019, 2023). Because the dust formed in ccSNe includes sufficiently large grains (0.1–0.5 μm), a significant fraction of the grains can survive (10%–20% for silicate dust and 30%–50% for carbon dust; Slavin et al. 2020).

Cas A is one of the youngest (∼350 yr) and closest ejecta-dominated SNRs and has been observed across all wavelengths, including optical (Fesen et al. 2006), X-ray (Hwang et al. 2004), radio (DeLaney et al. 2014), and infrared (Isensee et al. 2010, 2012; Smith et al. 2007). The progenitor mass of Cas A is still uncertain; it has been suggested it was a Wolf–Rayet star with a mass of 15–25 $M_{\odot}$ (Fesen 2001; Young et al. 2006). Spectra of a light echo from the SN that produced Cas A showed a Type IIb SN from the collapse of the helium core of a red supergiant that had lost most of its hydrogen envelope (Krause et al. 2008). Koo et al. (2020) alternatively suggest a blue supergiant precursor with a thin hydrogen envelope or a yellow supergiant (the progenitor mass is probably <15 $M_{\odot}$, depending on pre-SN mass loss).

Cas A is the best case study in the local Universe to understand dust formation in SN ejecta and shock-processing of freshly formed SN dust (De Looze et al. 2017). Spitzer infrared spectral mapping of Cas A confirmed that molecules and dust are present in the ejecta (Rho et al. 2008). Cas A also shows strong polarization fractions (∼20%) in the far-infrared, implying that the dust grains are large (Rho et al. 2023). CO was detected for the first time from the Palomar and Spitzer near-infrared (NIR) images (Rho et al. 2009, 2012). CO fundamental band features were detected in low-resolution AKARI spectra, showing that astrochemical processes and molecule formation continue to the stage of young SNRs (Rho et al. 2009, 2012).

Although CO molecules themselves are not on the immediate chemical path to dust formation (Sarangi & Cherchneff 2015), it is known that the detection of CO is an indication of molecular cooling and chemistry in the ejecta, leading to condensation of ejecta dust in later (from a few tens to a few hundred days after the explosion) epochs (Sarangi et al. 2018; Rho et al. 2018b, 2021). Although CO can form in the ejecta in early phases (∼100 days after SN explosion; Sarangi & Cherchneff 2013), the detection of later epoch CO has been associated with re-formation in the post-shock region (Biscaro & Cherchneff 2014), highlighting the complex and competing processes of molecular formation and destruction.

CO molecular lines have been observed in the late-time NIR spectroscopy of a number of SNe, e.g., two Type IIP SN1987A (Spyromilio et al. 1988) and SN 2017eaw (Rho et al. 2018a; Tinyanont et al. 2019) and a Type Ic SN2020oi (Rho et al. 2021). By comparing the production of molecules, ejecta, and dust at these early times to the molecular gas in Cas A, we can constrain both production and destruction of dust and molecules in SN explosions.

In this Letter, we present new observations of Cas A using JWST, focusing on NIRCam and MIRI imaging of the entire SNR and NIRSpec Integral Field Unit (IFU) observations of two selected filaments. JWST reveals that the CO-emitting regions mostly coincide spatially with the ejecta-dominated areas; however, the ratio between the CO and Ar ejecta varies across the SNR, and fine-scale differences in position and morphology exist between the CO emission and the ejecta. The NIRSpec spectra are dominated by complex CO bands and show a unique shape of the CO fundamental band.

2. Observations

We present JWST infrared observations of Cas A using NIRCam (Rieke et al. 2023), MIRI (Wright et al. 2023), and NIRSpec (Jakobsen et al. 2022). These observations were obtained as part of a Cycle 1 survey program on Cas A (Prog. ID of 1947), described in Milisavljevic et al. (2024). The NIRCam images were taken on 2022 December 5–6, using the F356W (3.140–3.980 μm) and F444W (3.880–4.986 μm) filters. The field of view (FOV) of NIRCam is $2\farcm2 \times 4\farcm4$ with the pixel scale of $0\farcs065$. In contrast, Spitzer images at these wavelengths have a spatial resolution of $3''$ (Fazio et al. 2004). We required a 2×3 mosaic to cover the full extent of Cas A. The NIRCam data required 1.9 hr on source exposure time for F345W and F444W images.

MIRI imaging using the F770W filter was taken multiple times between 2022 August 4 and October 26. The MIRI

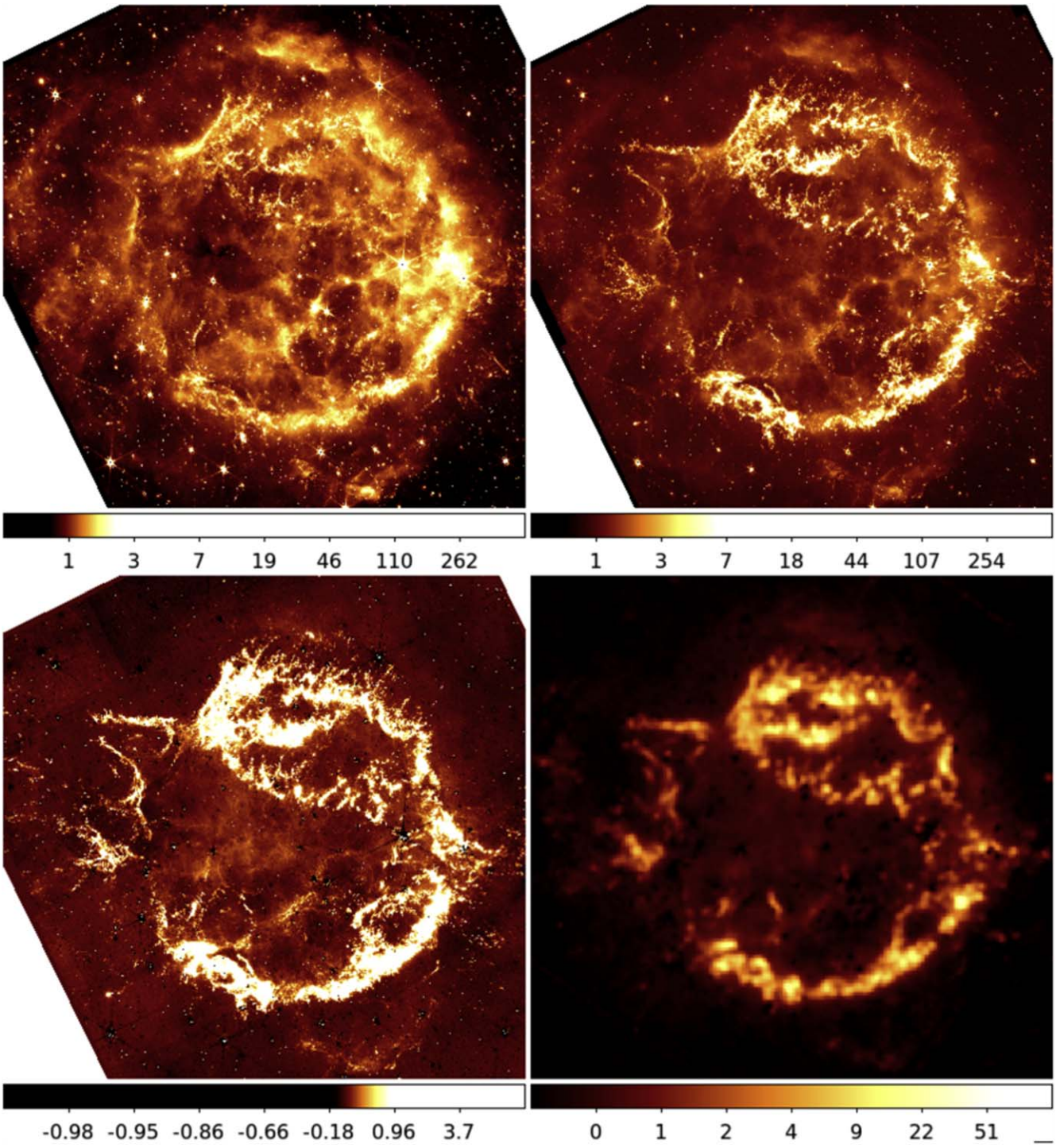

Figure 1. JWST F356W (3.56 μm; top left), F444W (4.44 μm; top right) images, CO fundamental image (produced from F444W image after subtracting the synchrotron emission using F356W image; bottom left), and equivalent CO image using Spitzer data (bottom right). The JWST images show far more complexity. The CO emission is from the CO fundamental bands and overlaps spatially with the knotty ejecta structures. Faint, extended, diffuse F444W emission seen in projection toward the center, hinted at with the Spitzer data, is more noticeable. The image is centered on R.A. $23^{h}23^{m}26\overset{s}{.}65$ and decl. $+58°49'14\overset{''}{.}98$ (J2000) with an FOV of $6\overset{'}{.}4 \times 6\overset{'}{.}4$. The units in the color bar are in MJy sr^{-1}.

imaging FOV is $1\overset{'}{.}23 \times 1\overset{'}{.}88$ with the pixel scale of $0\overset{''}{.}11$, requiring a 5×3 map to cover the SNR. The JWST mosaics were astrometrically aligned using the JWST Alignment Tool (Rest et al. 2023). The resulting aligned mosaics are shown in color in Figures 1 and 2.

Each NIRSpec-IFU position covers a region $3\overset{''}{.}7 \times 4''$ in size with $0\overset{''}{.}1$ pixels. Four IFU positions were observed for the program, as described in Milisavljevic et al. (2024). Here we focus on two positions that were observed, one on 2022 November 5 and the other on 2022 December 10. The position in the north (R.A. $= 350\overset{°}{.}873$, decl. $= 58\overset{°}{.}842$) targeted an ejecta knot, and the position in the south (R.A. $= 350\overset{°}{.}875$, decl. $= 58\overset{°}{.}790$) targeted a particularly bright region of CO emission. These positions (P1 and P3 in Milisavljevic et al. 2024) are shown in Figure 3. The other

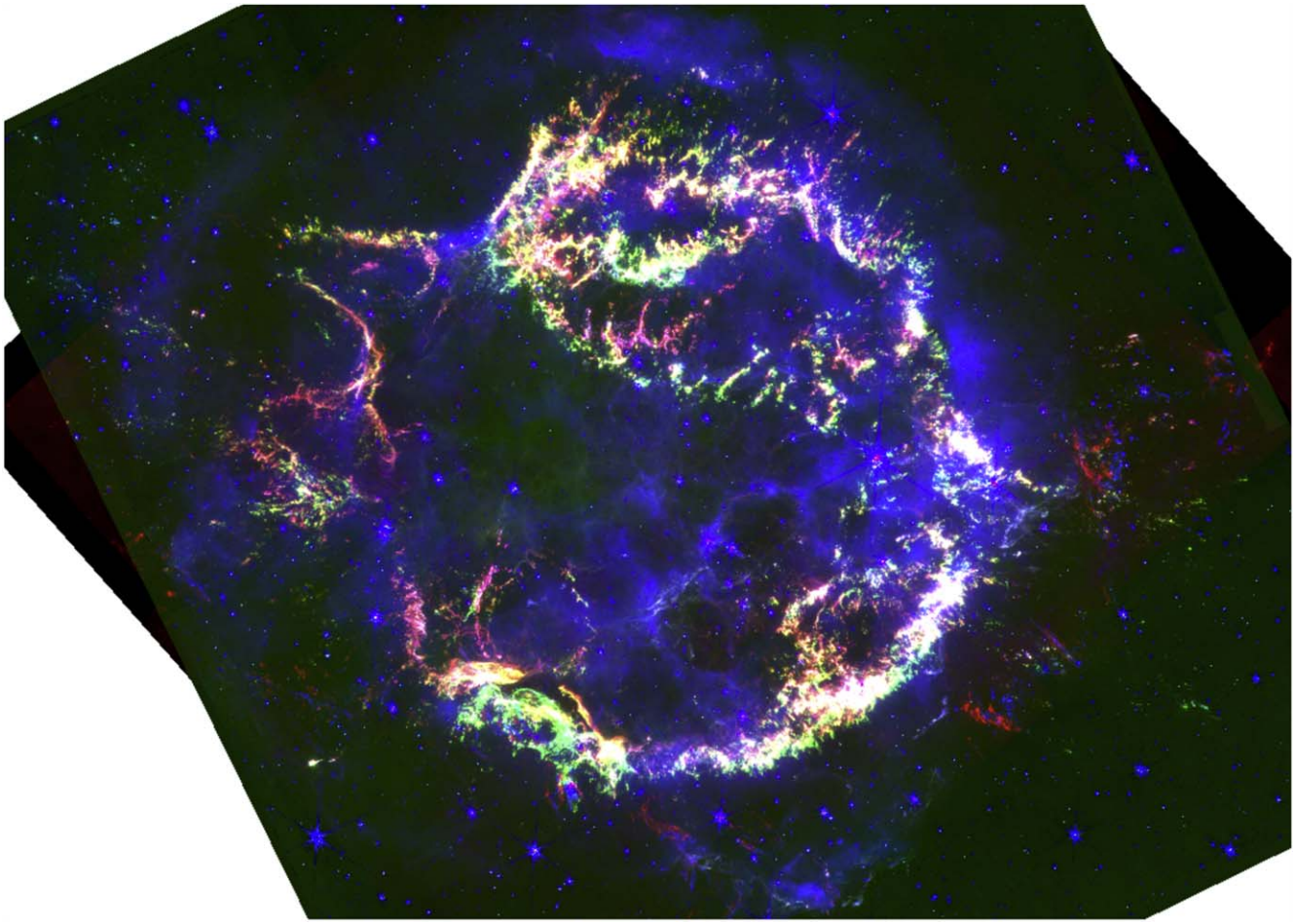

Figure 2. JWST three-color mosaicked images of synchrotron emission (F356W in blue), CO (synchrotron-subtracted F444W in green), and Ar ejecta (F770W in red). North is up, and east is to the left. The detailed structures of the three images are noticeably different from each other. The synchrotron emission (blue) shows smooth structures and is dominant outside the main shell.

two regions are reported by I. De Looze (2024, in preparation) and Milisavljevic et al. (2024). We extracted the JWST NIRSpec-IFU spectra from each pixel, and the total ∼1368 spectra are from 36 × 38 detector pixels. However, note that the IFU had 53 × 55 image size after World Coordinate System rotation. The effective integration and total exposure times are 145 and 583 s for the N field and 218 and 875 s for the S field, respectively. More details of the JWST observations of Cas A are described in Milisavljevic et al. (2024).

3. Results

3.1. Imaging

In Figure 1, we present the mosaicked NIRCam images. The top two panels show the separate JWST NIRCam mosaics from F356W and F444W. Much of the F356W emission appears relatively diffuse, similar to synchrotron radiation seen in the radio (Anderson et al. 1991), K-continuum (Rho et al. 2003), and Spitzer 3.6 μm (Rho et al. 2012) images. However, we note some knotty structures, likely ejecta, in the F356W image of the northern shell, which are visibly more compact and brighter than the synchrotron-emitting regions. The NIRSpec spectra also show a continuum from synchrotron emission, but at some locations the F356W band includes a [Ca IV] 3.2 μm line (see Figure 4 and Section 3.2 for details). Thus, while there may be isolated, localized contributions from ejecta emission, the F356W image mainly shows synchrotron emission.

The F444W image shows three main structures: (1) knotty structures from ejecta, (2) the forward-shocked material outside the bright shell, which shows a much smoother distribution, and (3) weak diffuse structures in the interior (see Figure 1). The NIRSpec-IFU spectra show CO emission is dominant (>99%) in compact knots and filaments, and the F444W filter also includes ejecta lines of [Si IX] at 3.94 μm, [Ca V] at 4.16 μm, [Mg IV] at 4.49 μm, [Ar VI] at 4.53 μm, and [K III] at 4.6 μm (see Section 3.2 for details). The F444W filter also includes synchrotron emission since the forward-shocked material is known to be from synchrotron emission, as seen in radio images (Anderson et al. 1991).

To remove the synchrotron component to first order and obtain a CO image, we scaled the F356W image to the F444W image assuming a synchrotron spectral index $\alpha = -0.68$ (Rho et al. 2003) where $\log S_\nu \propto \alpha \log \nu$ and subtracted it from the F444W image, which resulted in the lower left panel in Figure 1. This image is dominated by the inner ring of emission and should be due primarily to fundamental CO band emission, as previously suggested using Spitzer IRAC band 4 (at 4.5 μm) imagery and AKARI spectra (Rho et al. 2012); this will be confirmed and discussed further using NIRSpec in Section 3.2. The fourth panel in Figure 1 shows the Spitzer CO image for comparison (Rho et al. 2012). Individual CO structures in the

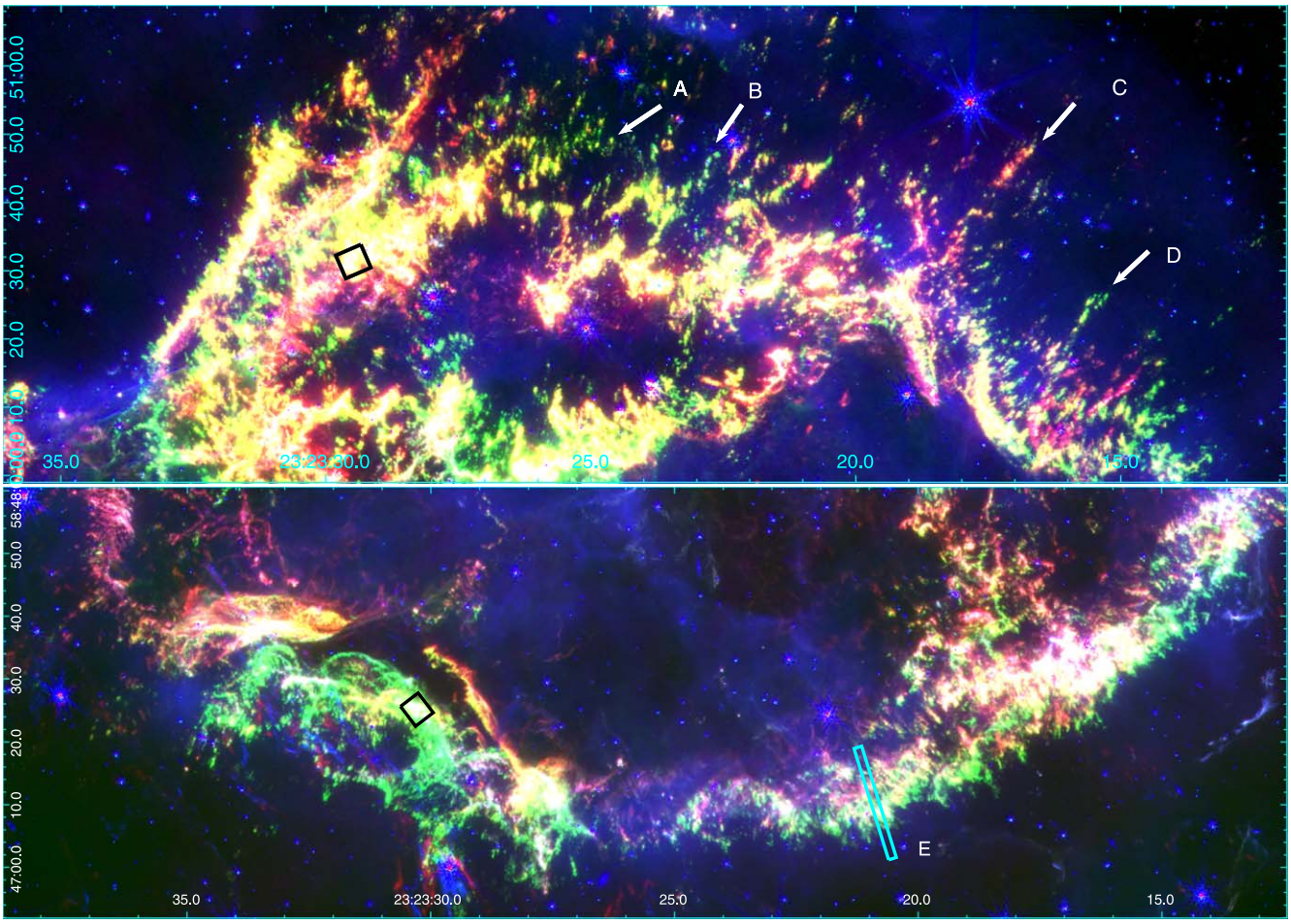

Figure 3. Zoomed-in images of Figure 2 on the northern (top) and southern (bottom) shells. The NIRSpec-IFU FOVs are marked as black squares on the JWST three-color images. The arrows point to the filaments showing CO excess emission (in green, marked as A, B, and D) and Ar ejecta excess (in red, marked as C). The slit (box E, in cyan) is cut through the southern shell where a radial profile is obtained in Figure 7.

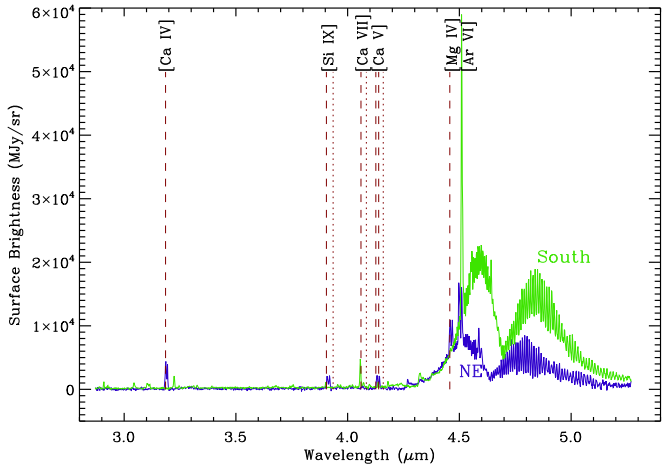

Figure 4. JWST NIRSpec-IFU spectra of Cas A toward two representative knots ($0\farcs1 \times 0\farcs1$ region for each) in the northern IFU field (R.A. = 350.°8731, decl. = 58.°8422 in blue) and at the southern IFU field (R.A. = 350.°8764, decl. = 58.°7905 in green). The spectra show a dominant CO fundamental band with a few high-ionization ejecta lines indicated. The two CO bumps arise from the R (the shorter wavelength bump) and P (the longer wavelength bump) branches of CO. The CO emission is stronger in the southern position, as expected from the imagery presented above. The ejecta lines are from [Ca IV] at 3.2 μm, [Si IX] at 3.94 μm, [Ca V] at 4.16 μm, [Mg IV] at 4.49 μm, [Ar VI] at 4.53 μm, and [K III] at 4.6 μm.

Spitzer image are resolved into numerous knots in the JWST images.

With this information in hand, we show the resulting aligned mosaics in color in Figure 2. Synchrotron (F356W) is shown in blue, fundamental CO emission (F444W after synchrotron subtraction) is shown in green, and the Ar ejecta emission (from [Ar II] at 6.98 μm) is shown in red. The Ar ejecta image is from the MIRI F770W data,k which cover 6.58–8.687 μm. The Spitzer spectrum shows that the Ar lines are dominant within these wavelengths (Rho et al. 2008; Smith et al. 2009). The synchrotron emission arises mainly from Fermi acceleration in the forward-shock region as it sweeps up and encounters interstellar medium/circumstellar medium (Rho et al. 2003). The three-color mosaicked images contrast synchrotron emission, CO molecules, and Ar ejecta emission in great detail on all scales all the way down to individual ejecta knots. While the ejecta and CO emissions both arise primarily in the bright ring of emission caused by the reverse shock, their spatial distributions are quite different from each other. Here we highlight two regions: the so-called "Ne-moon" regions (Figure 8 of Smith et al. 2009; Ennis et al. 2006) where the Ne emission is brighter than Ar emission; these are the two regions that appear in green and white in Figure 2.

We find that the spatial distribution of Ar (eastern region in red of Figure 2) and CO regions (northern and southern regions

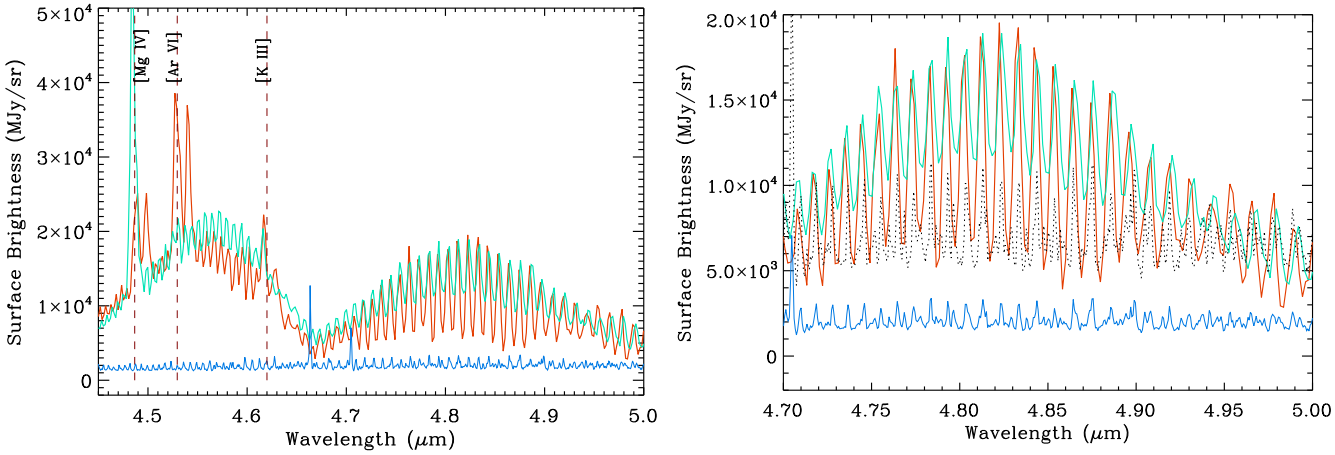

Figure 5. (Left) Two representative NIRSpec-IFU spectra from the northern shell (in orange) and southern shell (green) show dominant features from CO fundamental bands with a few high-ionization ejecta lines, in comparison with Orion (blue; Peeters et al. 2024). The northern spectra show two velocity components of −2070 and −1270 km s^{-1}, while the southern spectra show one component of +1060 km s^{-1}. The ∼3400 km s^{-1} difference between the blue- and redshifted motion of Cas A has been removed using the rest wavelengths of the ejecta lines. (Right) An enlarged section from the left panel shows a comparison of the lines with those of Orion (multiplied by 10, shown in dotted black.).

in green) is similar to the spatial distribution of different dust types identified by Rho et al. (2008; see Figure 3(f)): silicate (21 μm dust), carbon, and Al_2O_3 dust regions. These are zones of different nucleosynthesis and hence correspondingly very different in dust formation and composition. The CO regions are in He/O/C and O/C layers (zones 4A and 4B; Sarangi & Cherchneff 2013, 2015), and the Ar ejecta are in Si/O layers (zone 1B).

3.2. IFU NIR Spectroscopy

The positions of the NIRSpec-IFU apertures are shown in Figure 3, and representative extracted NIRSpec-IFU spectra are shown in Figures 4 and 5. These demonstrate the dominant nature of CO emission between 4 and 5 μm as well as the presence of other emission lines. The strongest ejecta lines are from [Ca IV] at 3.2 μm, [Si IX] at 3.94 μm, [Ca V] at 4.16 μm, [Mg IV] at 4.49 μm, [Ar VI] at 4.53 μm, and [K III] at 4.6 μm. The fundamental CO features are very bright from 4.2 to 5.3 μm and reveal unique shapes of CO, showing a few tens of sinusoidal patterns of rovibrational lines with pseudocontinuum underneath. There are many other faint lines that are yet to be identified, which is out of the scope of this Letter. There are strong lines of [Ar VI] 4.53 μm on the top of the CO feature. We also note the wavelength range within the MIRI F770W image is dominated by [Ar II] at 6.985 μm, which is 100–1000 times stronger than the continuum (Ennis et al. 2006; Rho et al. 2008; Smith et al. 2009).

The strongest detected lines and their properties are summarized in Table 1 with derived velocity information. In contrast with the previous Spitzer data where multiple velocity components were blended together, JWST resolves the knots in velocity space. The northern field shows pairs of blueshifted emission lines at velocities of −2000 and −1200 km s^{-1}. The southern field shows a single velocity component at +1600 km s^{-1}. The observed Doppler velocity structures are consistent with the 3D plot (Doppler velocity vs projected radius) of ejecta from the Spitzer Infrared Spectrograph (IRS) observations (Isensee et al. 2012; DeLaney et al. 2010). However, the JWST spectra reveal two reasonably well-separated Doppler-shifted groups of ejecta layers at −2000 and −1200 km s^{-1} in the northern filaments and a group of knots at +1600 km s^{-1} in the southern filament. Interestingly, all observed elements of Mg, Si, Ar, K, and Ca ejecta show similar velocity components.

A combination of the velocity shift and width indicates different nucleosynthetic layers. The two velocity shift components at −1200 and −2000 km s^{-1} for the NE region are likely caused by the different nucleosynthetic layers (see discussion by Isensee et al. 2012). However, the velocity width may be only a factor of 2–3 times larger than the instrumental spectral resolution (∼111 km s^{-1}), and yet its error is large (20%–100%). There may be some separation between these layers by a few hundred kilometers per second (corresponding to ∼5″ or ∼0.1 pc), and the width may indicate the physical size of the layer. For example, [Ca IV] layers are separated almost by ∼800 km s^{-1} (∼0.3 pc) between −2000 and −1200 km s^{-1} layers with each of ∼0.1 pc size, while the separation of [K III] layers is unclear due to the significant errors in the velocity widths.

We compare the NIRSpec spectra between the north and south regions in Figure 5. When we shift the spectra to align the features, we see a velocity shift of roughly 3400 km s^{-1} between the north and south. The north is blueshifted compared with the south and consistent with previous 3D reconstruction of the remnant (DeLaney et al. 2010; Milisavljevic & Fesen 2013). We also compared the forest of CO features in Cas A with those of the Orion nebula. Cas A's CO features are bright with prominent individual rovibrational features and show a broad underlying component, which we attribute to kinematic and instrumental broadening (see Section 4.2 for details). JWST spectra of the protoplanetary disk HH 48 also show CO features similar to Orion and Cas A but in absorption (Sturm et al. 2023).

We compare the NIRSpec spectra from a few regions. In Figure 6 we show spectra extracted from various subregions within the IFU fields. The locations of the spectral extraction regions are shown in the top panels Figures 6(a)–(d) and the color-coded spectra are shown in the panels below. The overall intensity and the contrast of the CO lines show variation, and variable strength ejecta lines are seen. The northern position spectra show more prominent ejecta lines than the southern region spectra.

Table 1
Observed Spectral Line Width and Brightness in the Two Representative Spectra

Region	Line	λ_0 (μm)	Wavelength (μm)	FWHM (μm)	Vel. Shift (km s^{-1})	Vel. Width (km s^{-1})	Line Brightness (10^{-3} erg s^{-1} cm^{-2} sr^{-1})
N	[Ca IV]	3.2067	3.1862 ± 0.0005	0.0059 ± 0.0013	−1918 ± 46	552 ± 122	7.970 ± 1.790
	[Ca IV]	3.2067	3.1937 ± 0.0005	0.0033 ± 0.0010	−1216 ± 47	309 ± 94	3.948 ± 1.196
N	[Si IX]	3.9357	3.9086 ± 0.0019	0.0069 ± 0.0047	−2065 ± 145	526 ± 358	2.669 ± 1.839
	[Si IX]	3.9357	3.9190 ± 0.0016	0.0052 ± 0.0038	−1151 ± 121	396 ± 290	2.123 ± 1.563
N	[Ca V]	4.1585	4.1315 ± 0.0016	0.0062 ± 0.0038	−1947 ± 115	447 ± 275	2.475 ± 1.531
	[Ca V]	4.1585	4.1419 ± 0.0013	0.0043 ± 0.0032	−1197 ± 94	310 ± 230	1.709 ± 1.261
N	[Mg IV]	4.4866	4.4583 ± 0.0019	0.0061 ± 0.0049	−1892 ± 70	407 ± 327	5.230 ± 4.109
	[Mg IV]	4.4866	4.4683 ± 0.0019	0.0047 ± 0.0046	−1223 ± 127	314 ± 307	3.587 ± 3.515
N	[Ar VI]	4.5295	4.4990 ± 0.0012	0.0073 ± 0.0028	−2020 ± 80	483 ± 185	11.160 ± 4.363
	[Ar VI]	4.5295	4.5105 ± 0.0010	0.0049 ± 0.0024	−1258 ± 1192	324 ± 150	7.048 ± 3.505
N	[K III]	4.6180	4.5870 ± 0.0046	0.0046 ± 0.0044	−2013 ± 278	298 ± 285	3.365 ± 4.970
	[K III]	4.6180	4.5985 ± 0.0067	0.0070 ± 0.0170	−1266 ± 435	454 ± 304	2.594 ± 6.279
S	UID[a]	...	3.1055 ± 0.0001	0.0086 ± 0.0003	...	830 ± 10[b]	2.020 ± 0.083
S	[Ca IV]	3.2067	3.2236 ± 0.0000	0.0050 ± 0.0001	+1581 ± 09	468 ± 10	2.922 ± 0.125
S	UID[a]	...	3.7547 ± 0.0002	0.0148 ± 0.0006	...	1182 ± 48[b]	0.861 ± 0.052
S	UID[a]	...	3.9024 ± 0.0001	0.0035 ± 0.0002	...	263 ± 15	0.642 ± 0.045
S	UID[a]	...	4.0570 ± 0.0000	0.0050 ± 0.0001	...	365 ± 8	4.082 ± 0.163
S	CO v = 1-0	...	4.3248 ± 0.0002	0.0100 ± 0.0004	...	634 ± 284[c]	3.053 ± 0.144
S	[Mg IV]	4.4866	4.5109 ± 0.0001	0.0063 ± 0.0002	+1619 ± 07	421 ± 13	39.080 ± 1.955
S	[K III]	4.6180	4.6421 ± 0.0003	0.0035 ± 0.0006	+1598 ± 18	231 ± 39	3.021 ± 0.707

Notes.
[a] UID indicates an unidentified line.
[b] The lines are broader, likely due to a contribution from another faint line(s).
[c] The line is broader because of contributions from a few rotational (J) transitions.

4. Discussion

4.1. Ejecta and CO Maps

We have examined the distribution of Ar, CO, and synchrotron emission, shown in Figure 2. Figure 3 shows an enlargement toward the bright northern and southern limbs, where CO emission can often be seen exterior to the Ar ejecta emission. Some examples of regions where enhanced CO emission lies at larger radii from the explosion center are marked with arrows A, B, and D in Figure 3 and box E in Figure 3. We have examined the CO and Ar emission morphology and found almost one-to-one correspondence between their emission, but CO emission is often shifted to appear at larger radii than the Ar emission. We quantified this using a radial profile cut across the southern shell (marked as Region E in Figure 3). The radial profiles of the cut across the southern shell in Figure 7 show that the peak in CO (dotted line in green) is located radially outward from that in Ar (dotted line in red). Synchrotron emission (in a blue curve) shows a weaker correlation with Ar ejecta and CO emission as its morphology differs from Ar and CO maps and knots.

Two scenarios are possible for the observation that the CO peak is offset outward from the Ar ejecta. The first scenario is that the CO molecules are re-forming behind the reverse shock, as suggested by Biscaro & Cherchneff (2014), as the shock propagates inwards. The other possibility is simply that Ar ejecta has cooled faster than CO, causing a lack of infrared emission of the Ar ejecta in the outskirts. In the reverse shock, the initial shock velocity is low and the gas density is high, so cooling may occur behind the shock wave (Chevalier 1977). Since the ejecta are at fairly high temperatures ($>10^6$ K), they may cool faster than the CO molecules.

However, the reverse shock moves rapidly as the density of expanding gas decreases, so the shock wave soon heats the gas to a temperature at which its cooling time is long. Only a few percent of the ejected mass may be cooled after the reverse shock has passed, as we observe ejecta knots in the far outer, high-velocity part of the shell (Fesen 2001). Most ejecta in the reverse shock remain at a high temperature, and the lack of ejecta emission relative to CO is not due to cooling of ejecta.

We compare the morphology of 4.5 μm (4.3–5.2 μm) CO images with the IFU images of [Ca IV] at 3.2 μm, [Si IX] at 3.9 μm, [Mg IV] at 4.5 μm, and [Ar VI] at 4.52 μm. Figure 8 shows separate ejecta distributions of Ca, Si, Mg, and Ar emission compared with CO emission in the northern NIRSpec-IFU position. The Mg map shows more emission in the northern part and different morphology than the others. The Si originates interior to the layers than C, O, or Mg. Figure 9 shows the spatial distribution of the two blueshifted (see Table 1) Mg emission components, color coded as blue and red in the figure; the blue-colored component stretched north to south, and the red-colored component stretches from southeast to northwest. Three color maps of [Mg IV], CO, and [Si IX] emission in Figure 9 show contrasting distributions, as the Si map differs from the other two. Figure 9 shows the southern IFU position, where again the Si map looks different from the CO and Mg ejecta emission distributions. The contrasting distribution of [Si IX] could be due to the fact that the [Si IX]

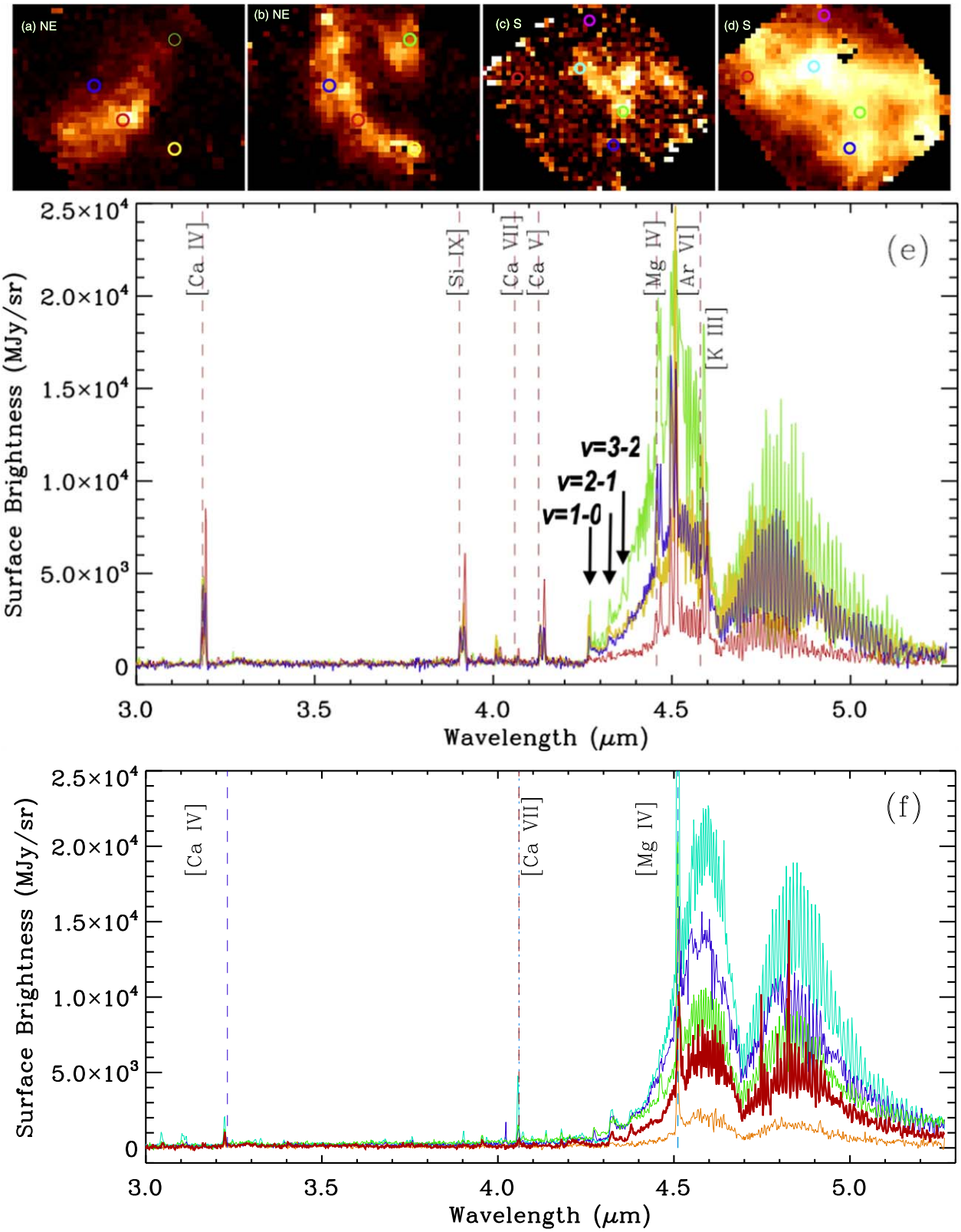

Figure 6. (Top) Regions for the extracted spectra shown below are marked on the images of NE IFU FOV for (a) 3.92 μm ([Si IX]), (b) 4.70 μm (CO), and of the S IFU FOV of (c) 3.92 μm ([Si IX]) and (d) 5.04 μm (CO). NIRSpec-IFU spectra of Cas A toward a few positions in the northern (middle: (e)) and south (bottom: (f)). The positions and marked circles on (a) and (b) and extracted spectra (e) are (R.A., decl.) = (350.°8724, 58.°8423) in green, (350.°8732, 58.°8421) in blue, (350.°8729, 58.°8419) in red, and (350.°8724, 58.°8418) in yellow. The positions and marked circles on (c) and (d) and extracted spectra (f) are (R.A., decl.) = (350.°8763, 58.°7907) in magenta ((c), (d)) or orange (f), (350.°8764, 58.°7904) in cyan, (350.°8771, 58.°7904) in red, (350.°8759, 58.°7902) in green, and (350.°8760, 58.°7900) in blue.

probably comes from a region of much lower density than the lower-ionization lines since the temperature is inversely proportional to the density (n_0) in a shock if the ram pressure is constant. More extensive IFU coverage of Cas A can help advance our understanding of the relative locations in ejecta, CO, and dust.

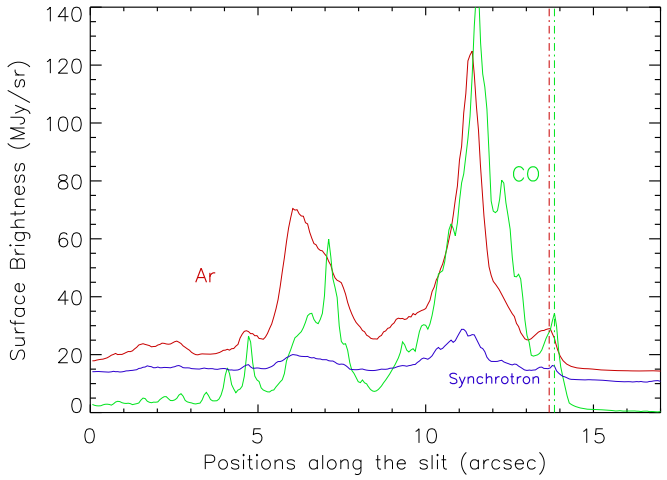

Figure 7. Profiles of surface brightness in Ar ejecta, CO, and synchrotron emission along a slit that cuts through the southern shell in an approximately radial direction (the slit is marked as box E in Figure 3, bottom panel). The position extends from (R.A., decl.) = (350.°838, 58.°789) to (350.°836, 58.°784). The CO peaks farther outward than the Ar emission. The vertical lines are peaks of Ar (in red) and CO emission (in green), respectively.

4.2. CO Modeling and Properties

The Cas A spectra in Figure 4 show two large rounded peaks corresponding to the R and P fundamental branches at 4.58 and 4.83 μm, respectively (Rho et al. 2012; see the discussion therein). The interval (wavelength difference) between R and P branch peaks depends on the temperature. The width between them is narrower for a lower temperature (Cami et al. 2010; Rho et al. 2012). The spectra show about 70 sawtooth-like CO spectral features in Figure 4. The contrast in the CO lines in the northern region spectra (red in Figure 5) is higher than that seen in the southern spectra (green). The CO spectral features largely correspond to specific $v = 1$–0 vibrational transitions from various rotational levels, J. Intrinsic and instrumental broadening of the lines blends then with weaker lines from $v = 2$–1 and higher vibrational states and with each other for higher J values in the R branch.

The CO fundamental lines have a similarity to the JWST spectra seen in the Orion nebula (blue in Figure 5), indicating similar individual CO features between Cas A and Orion. However, Cas A has much larger kinematic broadening, which changes the spectral appearance. The wings of the lines, and weaker lines, blend together to creating a pseudocontinuum. Recent JWST observations of HH 211 detect CO features (Ray et al. 2023), somewhat similar to those of Cas A, but its pseudocontinuum is not apparent like in Cas A. The projected dynamic velocity in HH 211 is 80–100 km s^{-1}, which can be the upper limit of the CO line width, and the line width is likely much less than that in Cas A.

We performed LTE model fitting based on Cami et al. (2010) and the CO molecular line data from Goorvitch (1994) to determine the physical conditions of CO molecules. This approach is similar to that used by Rho et al. (2012), Banerjee et al. (2016), and Rho et al. (2018a, 2021). We have quantified the goodness of fit (χ^2) for the models using the IDL routine MPFIT and the Python routines of MPFIT and LMFIT for the best-fitting parameters (Markwardt 2009). Before we compared with the CO LTE models, we shifted the velocity of the CO features to match the red- and blueshifted fine-structure line of [Ar VI] at 4.53 μm (we used the brighter component among the two velocity components). The northern and southern knots are blue- and redshifted, respectively. This shift allows the CO models to match the individual rovibrational lines.

Figure 10 shows the best fit of an LTE model with a temperature of 1078 (900–1250) K, a velocity width (FWHM) of 237 (160–350) km s^{-1}, and a column density of 3.8 (1–20) $\times 10^{17}$ cm^{-2}. The statistical errors are ~2%, but the errors include systematic errors by using different routines and methods. The intensities of the CO lines are well reproduced by the model, but the contrast in the lines is lower at higher J in the R branch, and the level of the pseudocontinuum falls well below the data at high J (the extreme long and short wavelengths of the emission). The spectral resolving power of the IFU is ~1000 at these wavelengths, which translates to a velocity resolution of ~111 km s^{-1}. However wider Gaussian profiles with a velocity width of 237 (160–350) km s^{-1} were able to reproduce the observed contrast of the CO lines and the blended emission underneath, as shown in Figure 10. Isolated far-IR CO rotational lines have shown similar velocity widths (Wallström et al. 2013). After we used line-width broadening, no extra smoothing was needed. The fundamental band is a combination of hundreds of individual lines, while the far-IR CO rotational lines are well isolated at each wavelength. The best-fit model (red in Figure 10) with a velocity width of 237 km s^{-1} has too little contrast in the lines compared to the observed spectrum (green in Figure 10) in the R-branch CO features (<4.67 μm), which suggests that a lower velocity width may be appropriate.

The ejecta and molecular knots have different density regions within them. The velocity width of ~237 km s^{-1} indicates that the CO gas is the post-shocked region of the reverse shock. The dense knots are compressed and fragmented by instabilities arising from the shock passage (Mellema et al. 2002; Raga et al. 2007; Silvia et al. 2010). The turbulence in dense knots is small, less than the turbulent velocity of 10 kms^{-1} in the warm gas (Korpi et al. 1999)

The observed velocity width of CO is the internal shock velocity that results from varying CO density and geometry (including the scales unresolved) that lead to variation in the shock speed and the direction with respect to the line of sight. The shock velocity in CO gas ($V_{\rm CO}$) is inversely proportional to the square root of the density ratio between CO ($n_{\rm CO}$) and ejecta ($n_{\rm ejecta}$) and proportional to the reverse shock velocity ($V_{\rm rs}$) ($V_{\rm CO} = V_{\rm rs} \times \sqrt{n_{\rm ejecta}/n_{\rm CO}}$) owing to the conservation of energy (Biscaro & Cherchneff 2014; Klein et al. 2003). The reverse shock velocity $V_{\rm rs}$ relative to the ejecta has beenestimated to be 2000–3000 km s^{-1} using optical data (Morse et al. 2004; Biscaro & Cherchneff 2014).

The reverse shock velocity in the ejecta can also be estimated from an X-ray gas temperature of 2.6 keV (~3×10^7 K; Hwang et al. 2004). The X-ray gas temperature $T^{\rm x}$ (= 3/16 $\mu/k\, V_{\rm rs}^2 \sim 11\, V_{\rm rs}^2$; references in Rho et al. 2021) infers V_{rs} of 1700 km s^{-1} (Equation 12–24 in Spitzer 1978) where μ is the mean mass per particle and k is the Boltzmann constant). The density of the ejecta is 10^{4-5} cm^{-3} (DeLaney et al. 2010), and the den- sity of CO gas is approximately 10^{6-7} cm^{-3} (Biscaro & Cherchneff 2014; Docenko & Sunyaev 2010). The critical density of CO ($n_{\rm crit} = A_{ul}/\gamma_{ul}$ where the Einstein A is the radiative transition, and γ is the collision coefficient between upper and lower levels) is high ($> 10^6$ cm^{-3}) for a temperature of 1000 K and an example of the upper and lower levels of v = 21 $\rightarrow$ 20^1. The observed velocity width of 237 (160–350) km s^{-1} is

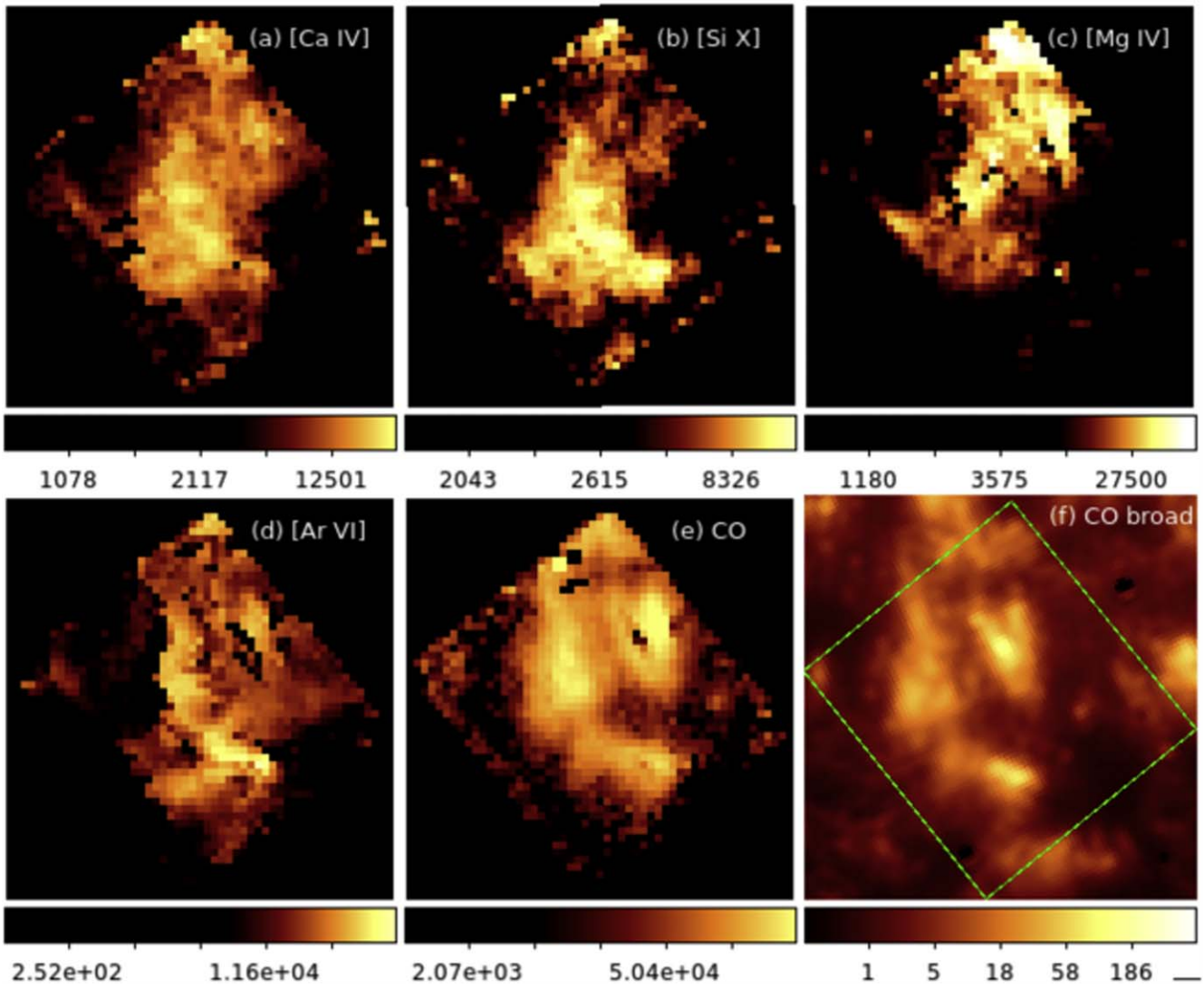

Figure 8. Cas A band images of the northern IFU field: (a) [Ca IV] at 3.2 μm, (b) [Si IX] at 3.9 μm, (c) [Mg IV] at 4.5 μm, (d) [Ar VI] at 4.52 μm, (e) CO 4.79 (4.788–4.798) μm, and (f) synchrotron-subtracted CO broad band (from F444W) images. The latter captures the brightest CO band. The CO emission appears similar to other ejecta maps.

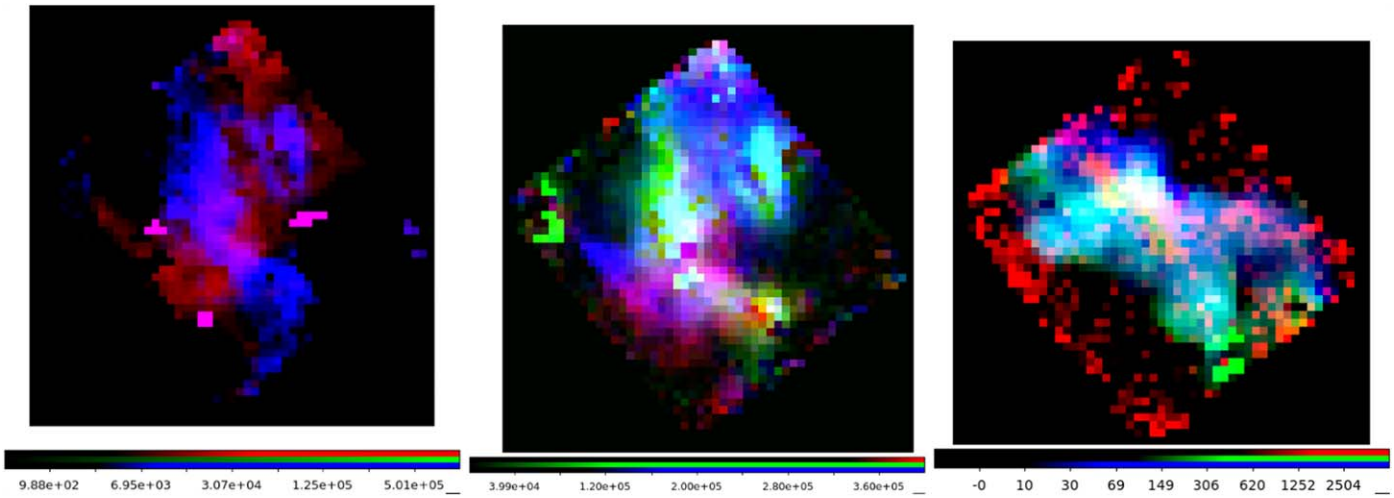

Figure 9. Cas A band images of the northern IFU field. (Left) Red and blue colors denote the two different kinematic components of [Ca IV] 3.2 μm in this field. (Middle) Three-color images showing [Mg IV] (in blue), CO (green), and [Si IX] (red). (Right) Three-color images of the southern IFU field: [Mg IV] (in blue), CO (green), and [Si IX] (red). CO and [Mg IV] show similar morphology, while [Si IX] morphology is different.

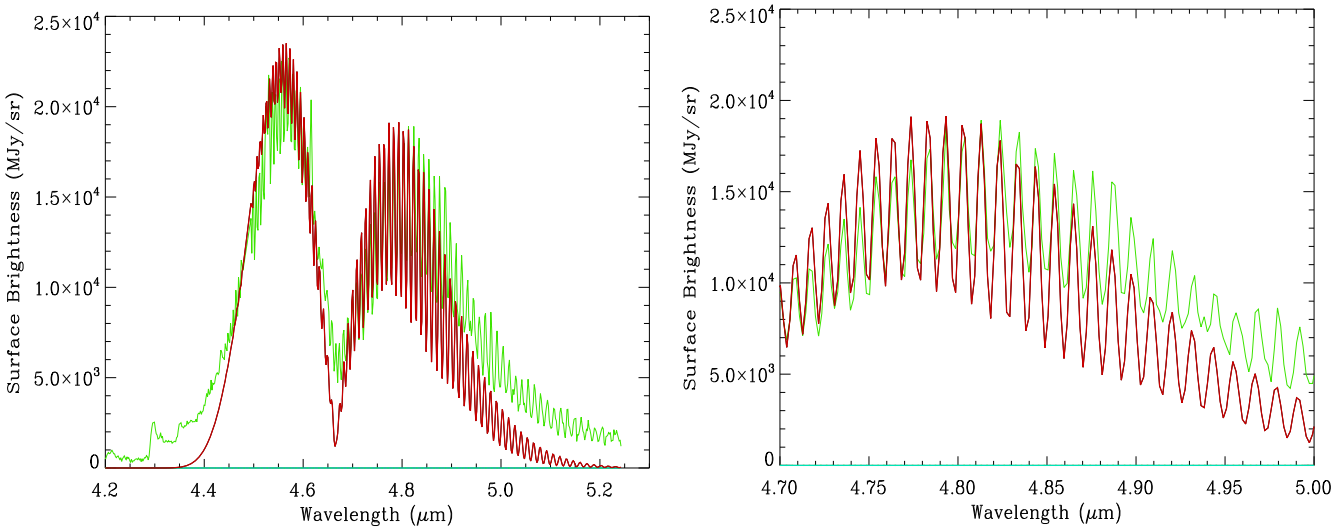

Figure 10. An LTE model (in red) using a temperature (T) of 1078 K and a velocity width of 200 km s^{-1} is superposed on the JWST southern region spectrum of Cas A (in green). The sawtooth-like patterns are reproduced, but the relative strengths differ slightly. In the expanded view in the expanded view of the spectra (Right), the peaks are from CO $v = 1$–0 P(4) through P(32) transitions. Blends with weaker $v = 2$–1 and higher vibrational states modulate the apparent contrast of the lines.

approximately the shock velocity inside the CO clumps of 170–300 km s^{-1} ($= 1700$–$3000 \times \sqrt{(5 \times 10^4)/(5 \times 10^6)}$).

The LTE model to reproduce the JWST spectra of Cas A only uses $^{12}C^{16}O$ without other CO isotopes. We simulated the intensity profile for optically thin and thick cases and found that the CO emission in Cas A was close to the optically thin case as it was found in the low-resolution AKARI spectra (Rho et al. 2012). The CO column density of 3.8 (1–20) $\times 10^{17}$ cm^{-2} is comparable to those obtained from the CO excitation diagram (Wallström et al. 2013). The high column density is consistent with the idea that CO molecules are re-formed behind the reverse shock (Wallström et al. 2013; Biscaro & Cherchneff 2014). The corresponding CO mass of the knot in the southern field is $\sim 2.3 \times 10^{-7}\, M_\odot$ per pixel (0.″1) at a distance of 3.4 kpc. Eventually, summing up all CO emissions from F444W emission and estimating the total CO mass from Cas A will be an interesting value. For that, JWST's advanced pipeline processing of individual frames is required, including removing hot pixels due to cosmic rays and various artifacts related to star subtraction, which is out of the scope of this Letter. The dip between the R and P branches (around 4.65 μm) from the LTE model is slightly off from the JWST spectra that were shifted based on ejecta lines. When we made a further shift of -0.014 μm (a total of 0.03 μm), the dip in the model was consistent with the JWST spectra of Cas A.

We notice a difference between the CO model and the JWST spectra at shorter and longer wavelengths as shown in Figures 10 and 11, which is much larger than the synchrotron emission ($\sim$5 MJy sr^{-1}). The synchrotron emission is an interpolation from radio fluxes, and detailed descriptions can be found in Rho et al. (2003, 2008, 2012). The emission could be due to dust emission. Therefore, we added a continuum component using carbon dust to the CO component and fit the spectrum. The results show the continuum at 4.8–5.2 μm has improved (the reduced χ^2 improved a factor 10), but the continuum fit did not improve the residuals between 4.25 and 4.4 μm.

An interesting feature of the Cas A CO spectra is the band heads that appear at $\sim$4.3 μm. These band heads are a rare detection. Starting from $J = 0$ at $\sim$4.6 μm, the wavelengths of

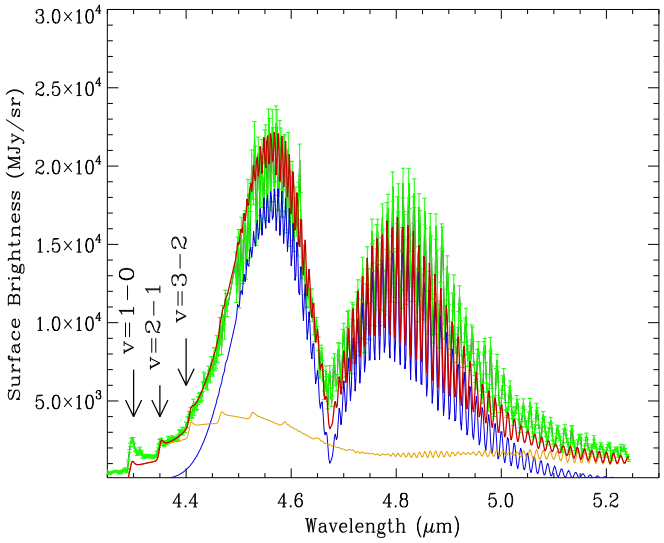

Figure 11. A two-temperature LTE CO model (in red) is superposed on the JWST southern spectrum of Cas A (in green). Here we have added a hotter CO component with $T = 4800$ K (yellow) and $\Delta V = 210$ km s^{-1} to the first-temperature component (blue). The total fit is shown in red. The band heads ($v = 1$–0, $v = 2$–1, and $v = 3$–2) are marked. The contribution of synchrotron emission is negligible about $\sim$50 MJy sr^{-1}, and wavelength dependence is small (the slope is 0.67).

successive R branch transitions get progressively shorter as J increases. However, the lines become increasingly closely spaced, and after $J \gtrsim 90$ the lines begin increasing in wavelength. The unresolvable pileup in wavelength of lines near $J \sim 90$ creates the band heads. Cas A spectra clearly show these band heads for at least three different vibrational transitions ($v = 1$–0 at 4.3 μm, $v = 2$–1 at 4.35 μm, and $v = 3$–2 at 4.45 μm), marked in Figure 6(e). The laboratory band-head wavelengths are $v = 1$–0 at 4.295 μm, $v = 2$–1 at 4.350 μm, v = 3–2 at 4.295 μm, and $v = 4$–3 at 4.465 μm (Geballe et al. 2007). The observed band heads are shifted by about -2000 km s^{-1} and $+1000$ km s^{-1} for the northern and southern region spectra, respectively, as we have previously

noted. The excitation energy of the $v = 0$ $J = 90$ level is about ~22,000 K, which implies that the temperature must be high for even a small fraction of the CO to be excited to such high v and J states. Therefore, the presence of such band heads may indicate multitemperature CO gas, or it may require a non-LTE model. We attempted to fit a two-temperature CO LTE model (with a second temperature component of 4800 K), shown in Figure 11 although the fit did not converge efficiently due to many small sinusoidal patterns and diverse combinations of two CO models. However, it demonstrates that the high-temperature CO model can reproduce the CO band heads at 4.3, 4.35, and 4.45 μm, indicating multiple temperature components of CO gas likely exist.

We also analyzed the CO excitation with the non-LTE radiative transfer code RADEX (van der Tak et al. 2007) as it was done by Wallström et al. (2013). The more sophisticated methods retain the assumption of a local excitation but solve for the balance of excitation and de-excitation rates from and to a given state, the so-called statistical equilibrium. The RADEX program was adapted for mid-infrared (MIR) and NIR CO emission (Wallström et al. 2013). While the model reproduced low-resolution CO AKARI spectra using temperatures of 400 and 2000 K, a velocity width of 300 km s^{-1}, and $N_{\rm CO}$ of 4×10^{17} cm^{-2}, it could not reproduce the CO sawtooth-like patterns seen in the JWST spectra. The contrast in the CO lines was much larger than in the JWST spectra (more than a factor of 5 stronger) when using a velocity of ~200–600 km s^{-1}, and increasing the velocity did not help reproduce the JWST spectra. The RADEX model produces asymmetrically oscillating CO patterns, which differ from the observed JWST spectra. The model, in particular, lacks CO emission below 4.5 μm and above 4.9 μm, which could be due to lack of H-atom collision partners or other missing collision rates. Future work on non-LTE modeling is encouraged to reproduce the JWST spectra of Cas A, which may need to include a large Doppler velocity broadening and various collision rates, including H-atom collision partners.

Non-LTE CO modeling can be preformed using the hydrodynamical radiation code (HYDRA), a hydrodynamic SN evolution code, including the nuclear networks and ejecta mixing, and Radiation code, accounting for the atomic-level population and the equations of state (see Hoflich et al. 1993; Rho et al. 2021). The γ-rays and free electrons at a certain temperature can ionize CO, which may affect the timescale of the CO and CO^+ formation and the ratio of CO^+ and CO. The time-dependent rate equations are $C + O \rightarrow CO$ and $C^+ + O \rightarrow CO^+$ (see also Liljegren et al. 2023; Ono et al. 2024). Nonthermal excitation can enhance CO^+, which adds a blueshifted emission component. NIR and MIR spectral signatures from CO only and from CO and CO^+ with and without nonthermal excitation for Type IC SNe are described in the appendix of Rho et al. (2021). Such complex HYDRA modeling for the progenitor Type IIB SN is encouraged and can be applied to the JWST spectra of Cas A.

5. Conclusion

In this Letter we have presented and analyzed JWST observations of the SNR Cas A to investigate the physical conditions for molecular CO formation and destruction in SN ejecta. Our conclusions can be summarized as follows:

1. NIRCam (F356W and F444W) and MIRI (F770W) images map synchrotron radiation, Ar-rich ejecta, and CO in great detail and reveal complex structures on the scale of individual ejecta knots. The CO map strongly correlates with knotty ejecta structures. CO is brightest in the northern and southern portions of the main shell and weakest in the east where ejecta emission dominates.
2. Complex fundamental bands of CO features dominate the NIRSpec-IFU spectra, with ~70 individually resolvable rovibrational lines. These lines are similar to those seen in the Orion nebula but with instrumental and velocity broadening in Cas A that blends lines to produce a pseudocontinuum.
3. LTE modeling of the CO spectra (R and P branches) suggests an optically thin CO gas with a temperature of ~1080 K, $N(\rm CO) = 4 \times 10^{17}$ cm^{-2}, $v = 200$ km s^{-1}, and $M_{\rm CO} = 2 \times 10^{-7}\, M_\odot$ per 0.″1 pixel.
4. We discover band heads for the $v = 1$–0, 2–1, and 3–2 rovibrational transitions at 4.3, 4.35, and 4.4 μm. The high rotational levels ($J \sim 90$) that need to be populated to form the band-head emission requires a high-temperature component in modeling the emission. When we fit the spectrum including a second CO component, the second temperature is ~4800 K, and the fitting favors a lower first-temperature component (i.e., lower than 1080 K), indicating the presence of multiple temperatures.

Acknowledgments

We thank the anonymous referee for the insightful comments. We thank Jan Cami, John Black, Sofia Wallstrom, and F. van der Tak for their assistance and discussion of CO LTE and non-LTE models. We thank Tom Geballe for the fruitful discussion regarding the various line transitions of CO molecules. This work is based on observations made with the NASA/ESA/CSA James Webb Space Telescope. Support for this program #1947 was provided by NASA through a grant from the Space Telescope Science Institute, which is operated by the Association of Universities for Research in Astronomy, Inc., under NASA contract NAS 5-03127. J.R. was supported by JWST-GO-01947.032 and was partially supported by a NASA ADAP grant (80NSSC23K0749) and Brain Pool visiting program for Outstanding Overseas Researchers by the National Research Foundation of Korea (NRF-2022H1D3A2A01096434). S.-H. P. and S.-C.Y. were supported by NRF-2019R1A2C2010885 and NRF-2022H1D3A2A01096434. R.G.A. was supported by NASA under award number 80GSFC21M0002. J.M.L. was supported by JWST grant JWST-GO-01947.023 and by basic research funds of the Office of Naval Research. H.-T. J. is grateful for support from the German Research Foundation (DFG) through the Collaborative Research Center "Neutrinos and Dark Matter in Astro- and Particle Physics (NDM)," grant No. SFB-1258-283604770, and under Germany's Excellence Strategy through the Cluster of Excellence ORIGINS EXC-2094-390783311.

ORCID iDs

J. Rho https://orcid.org/0000-0003-3643-839X
S.-H. Park https://orcid.org/0000-0001-7488-4337
R. Arendt https://orcid.org/0000-0001-8403-8548
M. Matsuura https://orcid.org/0000-0002-5529-5593
D. Milisavljevic https://orcid.org/0000-0002-0763-3885

T. Temim https://orcid.org/0000-0001-7380-3144
W. P. Blair https://orcid.org/0000-0003-2379-6518
A. Rest https://orcid.org/0000-0002-4410-5387
O. Fox https://orcid.org/0000-0003-2238-1572
A. P. Ravi https://orcid.org/0000-0002-7352-7845
B.-C. Koo https://orcid.org/0000-0002-2755-1879
M. Barlow https://orcid.org/0000-0002-3875-1171
A. Burrows https://orcid.org/0000-0002-3099-5024
R. Chevalier https://orcid.org/0000-0002-9117-7244
R. Fesen https://orcid.org/0000-0003-3829-2056
C. Fransson https://orcid.org/0000-0001-8532-3594
C. Fryer https://orcid.org/0000-0003-2624-0056
H. L. Gomez https://orcid.org/0000-0003-3398-0052
H.-T. Janka https://orcid.org/0000-0002-0831-3330
F. Kirchschlager https://orcid.org/0000-0002-3036-0184
S. Orlando https://orcid.org/0000-0003-2836-540X
D. Patnaude https://orcid.org/0000-0002-7507-8115
F. Priestley https://orcid.org/0000-0002-5858-6265
J. Raymond https://orcid.org/0000-0002-7868-1622
N. Smith https://orcid.org/0000-0001-5510-2424
J. Vink https://orcid.org/0000-0002-4708-4219
K. Weil https://orcid.org/0000-0002-8360-0831
J. Wheeler https://orcid.org/0000-0003-1349-6538
S. C. Yoon https://orcid.org/0000-0002-5847-8096

References

Anderson, M., Rudnick, L., Leppik, P., Perley, R., & Braun, R. 1991, ApJ, 373, 146
Banerjee, D. P. K., Srivastava, M. K., Ashok, N. M., & Venkataraman, V. 2016, MNRAS, 455, L109
Biscaro, C., & Cherchneff, I. 2014, A&A, 564, A25
Borkowski, K. J., & Shull, J. M. 1990, ApJ, 348, 169
Cami, J., Bernard-Salas, J., Peeters, E., & Malek, S. E. 2010, Sci, 329, 1180
Chawner, H., Marsh, K., Matsuura, M., et al. 2019, MNRAS, 483, 70
Cherchneff, I., & Dwek, E. 2009, ApJ, 703, 642
Cherchneff, I., & Lilly, S. 2008, ApJL, 683, L123
Chevalier, R. A. 1977, ARA&A, 15, 175
De Looze, I., Barlow, M. J., Swinyard, B. M., et al. 2017, MNRAS, 465, 3309
DeLaney, T., Kassim, N. E., Rudnick, L., & Perley, R. A. 2014, ApJ, 785, 7
DeLaney, T., Rudnick, L., Stage, M. D., et al. 2010, ApJ, 725, 2038
Docenko, D., & Sunyaev, R. A. 2010, A&A, 509, A59
Dwek, E., & Cherchneff, I. 2011, ApJ, 727, 63
Dwek, E., Sarangi, A., & Arendt, R. G. 2019, ApJL, 871, L33
Ennis, J. A., Rudnick, L., Reach, W. T., et al. 2006, ApJ, 652, 376
Fazio, G. G., Hora, J. L., Allen, L. E., et al. 2004, ApJS, 154, 10
Fesen, R. A. 2001, ApJS, 133, 161
Fesen, R. A., Hammell, M. C., Morse, J., et al. 2006, ApJ, 645, 283
Gall, C., Hjorth, J., & Andersen, A. C. 2011, A&ARv, 19, 43
Geballe, T. R., Rushton, M. T., Eyres, S. P. S., et al. 2007, A&A, 467, 269
Goorvitch, D. 1994, ApJS, 95, 535
Hoflich, P., Langer, N., & Duschinger, M. 1993, A&A, 275, L29
Hwang, U., Laming, J. M., Badenes, C., et al. 2004, ApJL, 615, L117
Isensee, K., Olmschenk, G., Rudnick, L., et al. 2012, ApJ, 757, 126
Isensee, K., Rudnick, L., DeLaney, T., et al. 2010, ApJ, 725, 2059
Jakobsen, P., Ferruit, P., Alves de Oliveira, C., et al. 2022, A&A, 661, A80
Kirchschlager, F., Schmidt, F. D., Barlow, M. J., De Looze, I., & Sartorio, N. S. 2023, MNRAS, 520, 5042
Kirchschlager, F., Schmidt, F. D., Barlow, M. J., et al. 2019, MNRAS, 489, 4465
Klein, R. I., Budil, K. S., Perry, T. S., & Bach, D. R. 2003, ApJ, 583, 245
Koo, B.-C., Kim, H.-J., Oh, H., et al. 2020, NatAs, 4, 584
Korpi, M. J., Brandenburg, A., Shukurov, A., & Tuominen, I. 1999, A&A, 350, 230
Kotak, R., Meikle, W. P. S., Farrah, D., et al. 2009, ApJ, 704, 306
Krause, O., Birkmann, S. M., Usuda, T., et al. 2008, Sci, 320, 1195
Laporte, N., Ellis, R. S., Boone, F., et al. 2017, ApJL, 837, L21
Liljegren, S., Jerkstrand, A., Barklem, P. S., et al. 2023, A&A, 674, A184
Markwardt, C. B. 2009, in ASP Conf. Ser. 411, Astronomical Data Analysis Software and Systems XVIII, ed. D. A. Bohlender, D. Durand, & P. Dowler (San Francisco, CA: ASP), 251
Matsuura, M., Dwek, E., Barlow, M. J., et al. 2015, ApJ, 800, 50
Matsuura, M., Dwek, E., Meixner, M., et al. 2011, Sci, 333, 1258
Mellema, G., Kurk, J. D., & Röttgering, H. J. A. 2002, A&A, 395, L13
Milisavljevic, D., & Fesen, R. A. 2013, ApJ, 772, 134
Milisavljevic, D., Temim, T., De Looze, I., et al. 2024, ApJL, 965, L27
Millard, M. J., Ravi, A. P., Rho, J., & Park, S. 2021, ApJS, 257, 36
Morse, J. A., Fesen, R. A., Chevalier, R. A., et al. 2004, ApJ, 614, 727
Niculescu-Duvaz, M., Barlow, M. J., Bevan, A., et al. 2022, MNRAS, 515, 4302
Nozawa, T., Kozasa, T., & Habe, A. 2006, ApJ, 648, 435
Nozawa, T., Kozasa, T., Habe, A., et al. 2007, ApJ, 666, 955
Nozawa, T., Kozasa, T., Umeda, H., Maeda, K., & Nomoto, K. 2003, ApJ, 598, 785
Ono, M., Nozawa, T., Nagataki, S., et al. 2024, ApJS, 271, 33
Peeters, E., Habart, E., Berne, O., et al. 2024, A&A, 685, 74
Priestley, F. D., Chawner, H., Matsuura, M., et al. 2021, MNRAS, 500, 2543
Raga, A. C., Esquivel, A., Riera, A., & Velázquez, P. F. 2007, ApJ, 668, 310
Ray, T. P., McCaughrean, M. J., Caratti o Garatti, A., et al. 2023, Natur, 622, 48
Rest, A., Pierel, J., Correnti, M., et al. 2023, arminrest/jhat: The JWST HST Alignment Tool (JHAT), v2, Zenodo, doi:10.5281/zenodo.7892935
Rho, J., Evans, A., Geballe, T. R., et al. 2021, ApJ, 908, 232
Rho, J., Gomez, H. L., Boogert, A., et al. 2018b, MNRAS, 479, 5101
Rho, J., Geballe, T. R., Banerjee, D. P. K., et al. 2018a, ApJL, 864, L20
Rho, J., Kozasa, T., Reach, W. T., et al. 2008, ApJ, 673, 271
Rho, J., Onaka, T., Cami, J., & Reach, W. T. 2012, ApJL, 747, L6
Rho, J., Ravi, A. P., Tram, L. N., et al. 2023, MNRAS, 522, 2279
Rho, J., Reach, W. T., Tappe, A., et al. 2009, ApJ, 700, 579
Rho, J., Reynolds, S. P., Reach, W. T., et al. 2003, ApJ, 592, 299
Rieke, M. J., Kelly, D. M., Misselt, K., et al. 2023, PASP, 135, 028001
Sarangi, A., & Cherchneff, I. 2013, ApJ, 776, 107
Sarangi, A., & Cherchneff, I. 2015, A&A, 575, A95
Sarangi, A., Matsuura, M., & Micelotta, E. R. 2018, SSRv, 214, 63
Shahbandeh, M., Sarangi, A., Temim, T., et al. 2023, MNRAS, 523, 6048
Silvia, D. W., Smith, B. D., & Shull, J. M. 2010, ApJ, 715, 1575
Slavin, J. D., Dwek, E., Mac Low, M.-M., & Hill, A. S. 2020, ApJ, 902, 135
Sluder, A., Milosavljević, M., & Montgomery, M. H. 2018, MNRAS, 480, 5580
Smith, J. D. T., Draine, B. T., Dale, D. A., et al. 2007, ApJ, 656, 770
Smith, J. D. T., Rudnick, L., Delaney, T., et al. 2009, ApJ, 693, 713
Spyromilio, J., Meikle, W. P. S., Learner, R. C. M., & Allen, D. A. 1988, Natur, 334, 327
Sturm, J. A., McClure, M. K., Beck, T. L., et al. 2023, A&A, 679, A138
Tinyanont, S., Kasliwal, M. M., Krafton, K., et al. 2019, ApJ, 873, 127
Todini, P., & Ferrara, A. 2001, MNRAS, 325, 726
van der Tak, F. F. S., Black, J. H., Schöier, F. L., Jansen, D. J., & van Dishoeck, E. F. 2007, A&A, 468, 627
Wallström, S. H. J., Biscaro, C., Salgado, F., et al. 2013, A&A, 558, L2
Wright, G. S., Rieke, G. H., Glasse, A., et al. 2023, PASP, 135, 048003
Young, P. A., Fryer, C. L., Hungerford, A., et al. 2006, ApJ, 640, 891